Frontiers in Bioscience Landmark

Front. Biosci. (Landmark Ed) **2023**; 28(11): 289
https://doi.org/10.31083/j.fbl2811289

Original Research

Comprehensive Analysis of Regulated Cell Death in Intracranial Aneurysms

Jianyu Zhu[1,2,3], Zhicheng Wang[1,2,3], Jiebo Li[1,2,3], Dezhi Kang[1,2,3,*]

[1]Department of Neurosurgery, National Regional Medical Center, Binhai Campus of the First Affiliated Hospital, Fujian Medical University, 350212 Fuzhou, Fujian, China
[2]Department of Neurosurgery, The First Affiliated Hospital, Fujian Medical University, 350005 Fuzhou, Fujian, China
[3]Fujian Institute of Neurology, The First Affiliated Hospital, Fujian Medical University, 350005 Fuzhou, Fujian, China
*Correspondence: kdz99988@vip.sina.com (Dezhi Kang)
Academic Editors: Sung Eun Kim and Viviana di Giacomo
Submitted: 23 March 2023 Revised: 25 June 2023 Accepted: 5 July 2023 Published: 16 November 2023

Abstract

Background: Abnormalities in regulated cell death (RCD) are involved in multiple diseases. However, the role of RCD in intracranial aneurysms (IA) remains unknown. The aim of this study was to explore different RCD processes in the pathogenesis of IA. **Methods**: Four microarray datasets (GSE75436, GSE54083, GSE13353, GSE15629) and one RNA sequencing (RNA-seq) dataset (GSE122897) were extracted from the Gene Expression Omnibus (GEO) database. The microarray datasets were merged to form the training set, while the RNA-seq dataset was used as the validation set. Differentially expressed genes (DEGs), gene set enrichment analysis (GSEA), and gene set variation analysis (GSVA) were used to investigate the role of different types of RCD, including apoptosis, necroptosis, autophagy, ferroptosis and pyroptosis in the formation of IA. A novel cell death classification system for IA was established using an unsupervised consensus clustering algorithm based on cell death signature genes. Differences in functional enrichment, cell death-related regulators, and immune infiltration between two cell death clusters were evaluated. Finally, predictive genes were identified using the least absolute shrinkage and selection operator (LASSO) regression, random forest and logistic regression, allowing a prediction model to be constructed for IA rupture. **Results**: Multiple RCD processes were significantly activated in IAs compared to controls. A total of 33 signature genes related to cell death were identified. The IA samples were divided into two clusters based on the cell death signature. The cell death-high subtype had a relatively higher rate of rupture, and higher enrichment levels for multiple cell death processes and several signal transduction and immune-related pathways. Immune infiltration analysis showed that cell death scores were correlated with multiple immune cell types, including macrophages, mast cells, T cells and B cells. A six-gene prediction model was constructed to predict rupture. The area under curves (AUCs) for predicting rupture in the training and validation cohorts were 0.924 and 0.855, respectively. **Conclusions**: Comprehensively analysis of RCD in IA and found that multiple RCD types are likely to be involved in IA formation and rupture. These cell death processes were correlated with inflammation and immunity. We present novel insights into the mechanism of IA pathogenesis that should help to guide further research.

Keywords: intracranial aneurysm; regulated cell death; rupture; inflammation; immunity

1. Introduction

Intracranial aneurysms (IA) are abnormal bumps on the intracranial wall and the most common cause of subarachnoid hemorrhage (SAH). The overall mean prevalence of unruptured IAs has been estimated to be 2.8% (95% CI, 2.0%–3.9%), with a mean age of 50 years [1]. Ruptured IAs can result in devastating SAH, with a mortality of approximately 50% and neurologic morbidity in 30%–50% of survivors [2]. Interventional endovascular management and microsurgical clipping are still the main methods used to treat IA [3]. However, the risks and potential complications of surgery cannot be ignored, and some patients may not tolerate surgical treatment. Additionally, the detection rate for unruptured IAs is increasing due to advances in imaging techniques. Therefore, for patients with high-risk IA and those who cannot tolerate surgical treatment, noninvasive treatments such as pharmacotherapy and targeted therapy are promising methods for preventing the progression and rupture of IAs [4–8]. In order to find an effective therapeutic strategy, it is important to understand the pathophysiological mechanisms of IA formation and rupture.

The initiator of endothelial dysfunction is hemodynamic stress. Macrophage-activated inflammation is considered to be a pivotal event in the formation, progression and rupture of IA. The inflammatory response and the release of matrix metalloproteinases (MMPs) lead to degeneration of the extracellular matrix (ECM) and phenotypic modulation of vascular smooth muscle cells (VSMC). This eventually results in apoptosis of VSMCs and the formation of aneurysms [9–12]. VSMC apoptosis is therefore a characteristic feature of IA. Abnormalities in regulated cell death (RCD) processes, including apoptosis and nonapoptotic cell death, have been observed in the pathogenesis of various diseases [13,14]. Apoptosis in the aneurysm walls has been widely reported in patients with IA [15–18]. Al-

though apoptotic cell death is closely associated with inflammation and immunity [14,19], the role of non-apoptotic cell death in IAs has not yet been elucidated.

The aim of the present study was therefore to explore the contribution of various types of cell death in the pathogenesis of IA, including apoptosis, necroptosis, autophagy, ferroptosis and pyroptosis. We found that multiple types of cell death were involved in IA formation. Furthermore, patients with IA were clustered according to their cell death-related signature genes. This identified two subtypes of cell death related to rupture, immune infiltration, and inflammation. Subsequently, we constructed a prediction model that was able to predict IA rupture. Our findings indicate a potential connection between various cell death processes and the formation and rupture of IAs. These results provide novel insights into the non-surgical therapy of IAs.

2. Materials and Methods

2.1 Data Acquisition and Preprocessing

The workflow chart showing the study design is presented in Fig. 1. Five datasets of IA were obtained from the Gene Expression Omnibus (GEO) database (https://www.ncbi.nlm.nih.gov/geo/), including four microarray datasets (GSE75436, GSE54083, GSE13353, GSE15629) and one RNA sequencing (RNA-seq) dataset (GSE122897). Details of the selected datasets are shown in **Supplementary Table 1**. Raw data from the four microarrays were merged. Batch effects were removed by package "SVA" [20], and data normalization was implemented by package "limma" in R [21] (**Supplementary Fig. 1**). Corresponding clinical data were obtained from the appropriate metadata within the GEO database. The merged microarray data were used as the training set, and the RNA-seq data used as the validation set.

2.2 Identification of Differentially Expressed Genes

Differentially expressed genes (DEGs) were identified using the empirical Bayesian approach of the "limma" package [21]. Genes with $p < 0.05$ and |log2 fold change (FC)| >0.5 between IA samples and control artery samples were considered to be DEG. The "pheatmap" package was used to draw heatmaps, and the "ggplot2" package used to draw volcano plots. The overlap of DEGs between the microarray and the RNA-seq datasets was shown using the "VennDiagram" package.

2.3 Cell Death Processes Enrichment Analysis

Gene set enrichment analysis (GSEA) is a method to assess the distribution trend of genes in a predefined set [22]. In the present study, GSEA was used to assess the contribution of different cell death pathways to IA formation. The apoptosis, necroptosis, autophagy and ferroptosis pathways were downloaded from the Kyoto Encyclopedia of Genes and Genomes (KEGG) database (https://www.kegg.jp/), and the pyroptosis gene sets were downloaded from the Molecular Signatures Database (MSigDB) (http://www.gsea-msigdb.org/gsea/msigdb/index.jsp). GSEA was performed using the "ClusterProfiler" package and visualized using the "enrichplot" package. The threshold was set to an adjusted p (p.adj) < 0.05. Gene set variation analysis (GSVA) was performed using the "GSVA" package to quantify the expression levels of various cell death pathways in all samples [23]. A $p < 0.05$ was considered to indicate statistical significance between the IA and control groups. We also used the "Pathview" R package to visualize the relative expression levels of key genes in the KEGG pathways of apoptosis, necroptosis, autophagy and ferroptosis in IA samples [24]. In addition, the major positive and negative regulators of apoptosis, necroptosis, autophagy, ferroptosis and pyroptosis were obtained from the previous literature (**Supplementary Table 2**) [13,14,19]. The different expression levels of these regulators between the IA and control samples were visualized by heatmaps.

2.4 Identification of Molecular Subtypes Based on Cell Death Signature

Enrichment analysis suggested that multiple cell death pathways were enriched in the IA samples. Therefore, we constructed an integrative classification of regulated cell death. The sets of apoptosis, necroptosis and pyroptosis genes were downloaded from MSigDB, the autophagy-related genes were downloaded from the Human Autophagy Database (HADb) (http://www.autophagy.lu/), and the ferroptosis-related genes were downloaded from FerrDb V2 (http://www.zhounan.org/ferrdb/current/). The various types of cell death-related genes were intersected with DEGs separately to obtain the cell death signature genes.

To further identify different IA patterns related to cell death signature genes, an unsupervised consensus clustering algorithm was applied with the k-means method using the "ConsensusClusterPlus" package [25]. Clustering was iterated 1000 times to ensure the stability of the classification. The optimal number of clusters was determined by the relative changes in the area under the cumulative distribution function (CDF) curves of the consensus score and the consensus heatmap. The novel cell death classification was visualized and verified using a principal component analysis (PCA) with the "factoextra" package. Single sample GSEA (ssGSEA) was applied to quantify the enrichment level of the set of cell death signature genes for each sample using the "GSVA" package. ssGSEA scores were defined as cell death scores.

2.5 Determination of DEGs in Different Cell Death Clusters

DEGs were screened using the "limma" package in two cell death clusters. $p < 0.05$ and |log2 FC| >1 were defined as the threshold for differential expression of genes between two clusters. The results of differential

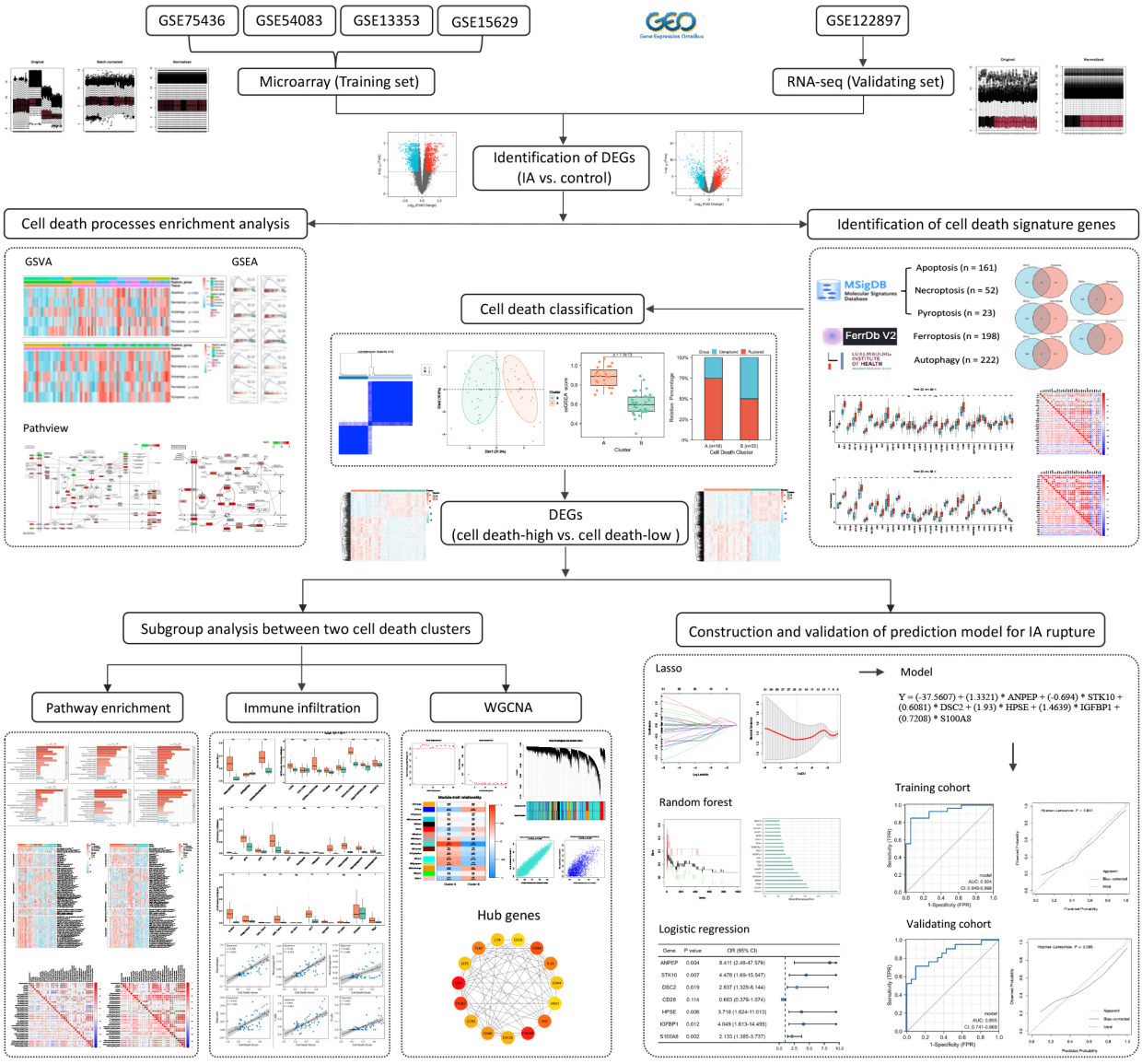

Fig. 1. Workflow chart. IA, intracranial aneurysm; DEG, differentially expressed gene; WGCNA, weighted gene co-expression network analysis.

gene expression were displayed using volcano graphs and heatmaps. The overlapping DEGs identified in the microarray and RNA-seq datasets were shown in Venn diagrams.

2.6 Functional Enrichment Analysis Between Different Cell Death Clusters

The "ClusterProfiler" R package was used to perform Gene Ontology (GO) functional and KEGG pathway enrichment analysis of the newly identified DEGs [26]. Significantly enriched functions and pathways were selected with an adjusted *p*-value (*p*.adj) < 0.05 and false discovery rate (FDR) <0.2. To comprehensively explore differentially expressed levels of various signaling pathways in the two cell death patterns, the pathways for cell growth and death, signal transduction, signaling molecules and interaction, and immune system were downloaded from the KEGG database. The GSVA was implemented and the GSVA scores of different signaling pathways between the two cell death clusters were compared using the "limma" tool. A *p*.adj < 0.05 was considered to indicate statistical significance. Furthermore, the differentially expressed levels of the main regulators of various cell death types between two clusters were compared by the "limma" package.

2.7 Immune Cell Infiltration

The algorithms "MCPcounter" [27] and "xCell" [28] were used to examine the immunocyte infiltration of IAs. The immune cell composition of patients with different cell death clusters was compared and shown in boxplots. Correlations between cell death scores and the infiltration levels of different immune cell types were analyzed using Spearman correlation analysis.

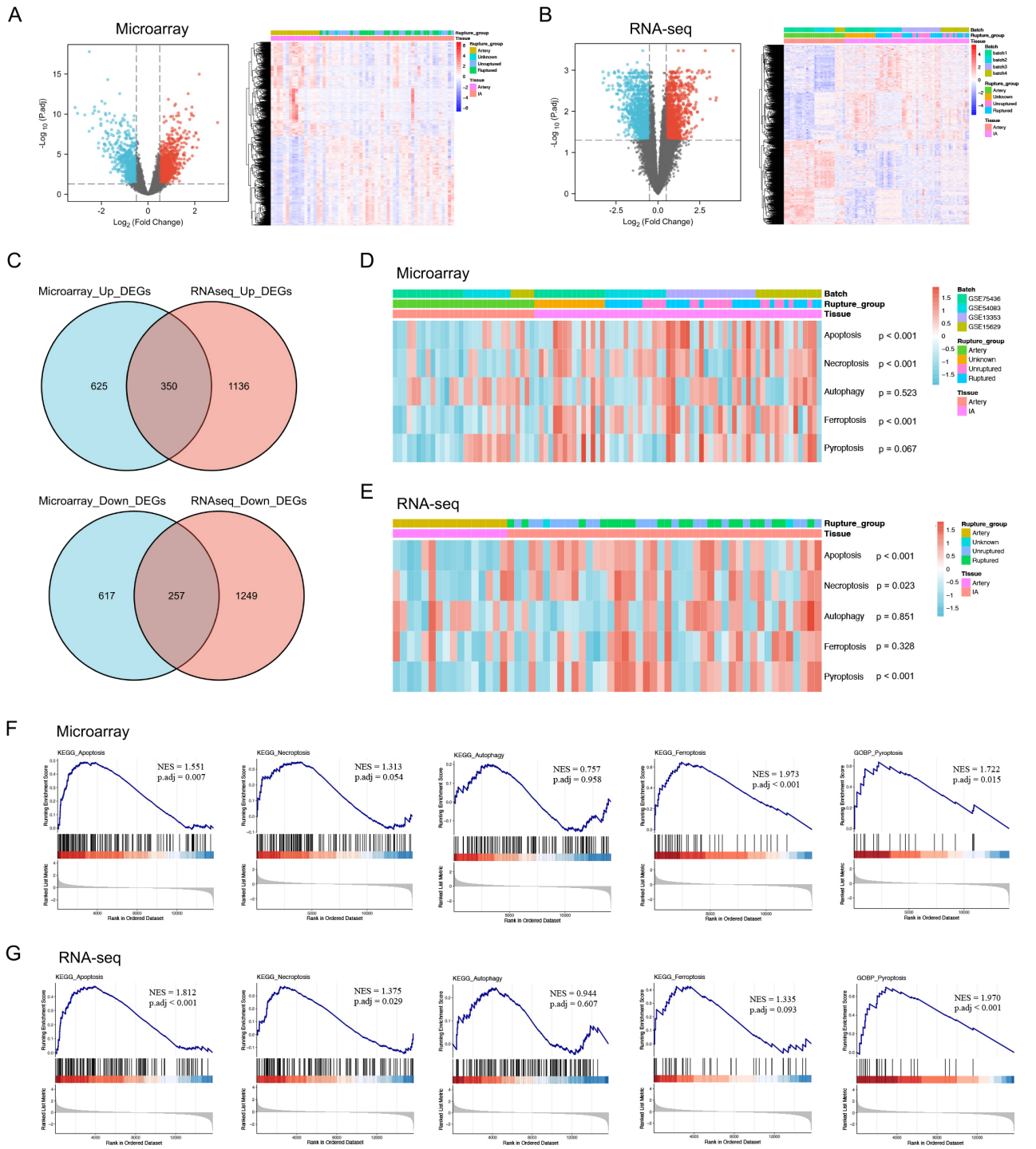

Fig. 2. Identification of differentially expressed genes (DEGs) and analysis of cell death enrichment. (A) Volcano plot and heatmap of DEGs identified in the microarray set. (B) Volcano plot and heatmap of DEGs identified in the RNA-seq set. (C) Venn diagram of DEGs. (D,E) Gene set variation analysis (GSVA) of cell death pathways. (F,G) Gene set enrichment analysis (GSEA) of cell death pathways.

2.8 Weighted Gene Co-Expression Network Analysis

Weighted gene co-expression network analysis (WGCNA) was performed using the "WGCNA" R package to determine the gene modules linked to the different cell death patterns [29]. The WGCNA network was first constructed using a scale-free topology network with an optimal soft threshold. The relationship between the gene modules and two cell death clusters was then evaluated by Spearman correlation analysis and shown in heatmaps. The genes in the module with the strongest correlation with cluster A were imported into

the STRING database (https://cn.string-db.org/). The protein-protein interaction (PPI) network was obtained with high confidence (minimum required interaction score = 0.700) and visualized using Cytoscape software (version 3.9.1, https://cytoscape.org/, GitHub Inc, San Francisco, CA, USA). Finally, the CytoHubba plugin was used to determine the hub proteins in the PPI network via the degree algorithm.

2.9 Construction and Validation of a Prediction Model for IA Rupture

The merged microarray dataset was used as the training set, and the RNA-seq dataset was used as the validation set. The DEGs identified between two cell death clusters were used for screening. First, the least absolute shrinkage and selection operator (LASSO) technique and random forest (RF) algorithm were used to eliminate redundant variables. The optimal parameter with the lowest error rate and the best stability tree number was determined by calculating the error rates for 1 to 1000 trees. The Gini coefficient method was applied to evaluate the importance of the variables through RF. Univariate logistic regression was then performed to further select valuable predictive genes for IA rupture. The generalized linear model was finally used to develop a prediction model of IA rupture. The predictive performance of the generalized linear model was measured by the concordance index (C index) and receiver operating characteristic (ROC) curves [30]. Calibration was evaluated using a calibration plot [31]. The goodness of fit of the model was assessed by the Hosmer-Lemeshow (HL) test. LASSO regression, logistic regression, and generalized linear model were conducted using the "glmnet" R package. The random forest was carried out using the "random Forest" package in R. ROC curves were performed using the "pROC" package.

2.10 Statistical Analysis

All of the statistical analysis was performed in R (version 4.2.1, https://www.r-project.org, the Comprehensive R Archive Network, Vienna, Austria). Continuous data were expressed as means $\pm$ standard deviations (SDs), or quartiles (medians [25th percentiles, 75th percentiles]), while categorical data were summarized as frequencies and percentages. Student's t test or the Wilcoxon test were used for pairwise comparison between two groups. The statistical significance in all of the analyses was assumed to be $p < 0.05$.

3. Results

3.1 Profiles of DEGs

The merged microarray dataset included 61 IA and 30 control samples. The RNA-seq dataset included 44 IA and 16 control samples. The microarray cohort contained 27 ruptured IAs and 19 unruptured IAs, with the rupture status of the remaining 15 IA samples being unknown. The RNA-seq cohort contained 21 ruptured IAs, 21 unruptured IAs, and two IAs with unclear rupture status. A total of 1849 DEGs were identified in the microarray dataset, including 975 upregulated genes and 874 downregulated genes. In the RNA-seq dataset, 1486 upregulated DEGs and 1506 downregulated DEGs were identified. Volcano plots and heatmaps were used to visualize the expression of DEGs in all cases (Fig. 2A,B). The Venn diagrams show the intersection of DEGs between the microarray and RNA-seq datasets. These yielded 350 upregulated DEGs and 257 downregulated DEGs (Fig. 2C).

3.2 Cell Death Processes Enrichment Analysis

GSEA and GSVA were performed to explore the role of various types of RCD in IA formation. GSVA results in the microarray cohort showed that apoptosis, necroptosis, and ferroptosis expression levels were significantly higher in the IA samples than in controls (Fig. 2D). In the RNA-seq dataset, apoptosis, necroptosis, and pyroptosis showed higher expression in IA than in control samples (Fig. 2E). In the microarray dataset, GSEA revealed that IAs were significantly enriched in apoptosis, ferroptosis and pyroptosis-related pathways (Fig. 2F). In the RNA-seq set, DEGs were markedly enriched in apoptosis, necroptosis and pyroptosis (Fig. 2G). The relative expression levels of key genes in the apoptosis, necroptosis, autophagy, and ferroptosis pathways were visualized using pathview plots (**Supplementary Fig. 2**). The expression levels of multiple positive regulators of cell death were higher in IAs than in controls, while several negative regulators were downregulated in IAs (Fig. 3A,B).

3.3 Identification of Cell Death Signature

Functional enrichment analysis showed that multiple types of cell death were involved in IA. Therefore, we further investigated the cell death signature genes associated with IA. Firstly, we downloaded 161 apoptosis-related genes, 52 necroptosis-related genes, and 23 pyroptosis-related genes from the MSigDB database, as well as 222 autophagy-related genes from the HADb database and 198 ferroptosis-related genes from the FerrDb V2 database. Next, we obtained the overlapping genes by intersecting various cell death-related genes and the DEGs between IAs and controls (Fig. 4A). In total, we identified 15 signature genes related to apoptosis, 5 to necroptosis, 11 to autophagy, 8 to ferroptosis, and 2 to pyroptosis (Fig. 4A). After the removal of duplicates, a total of 33 cell death signature genes were identified. All showed increased expression in IA samples compared to controls, except for ITPR1, EGFR, LIFR and CPEB1 (Fig. 4B,C). Spearman correlation analysis also showed the expression of most of these cell death signature genes was positively correlated with each other (**Supplementary Fig. 3**). Signature genes were uploaded to the STRING database and the PPI network was visualized using Cytoscape software (Fig. 4D). The top 10

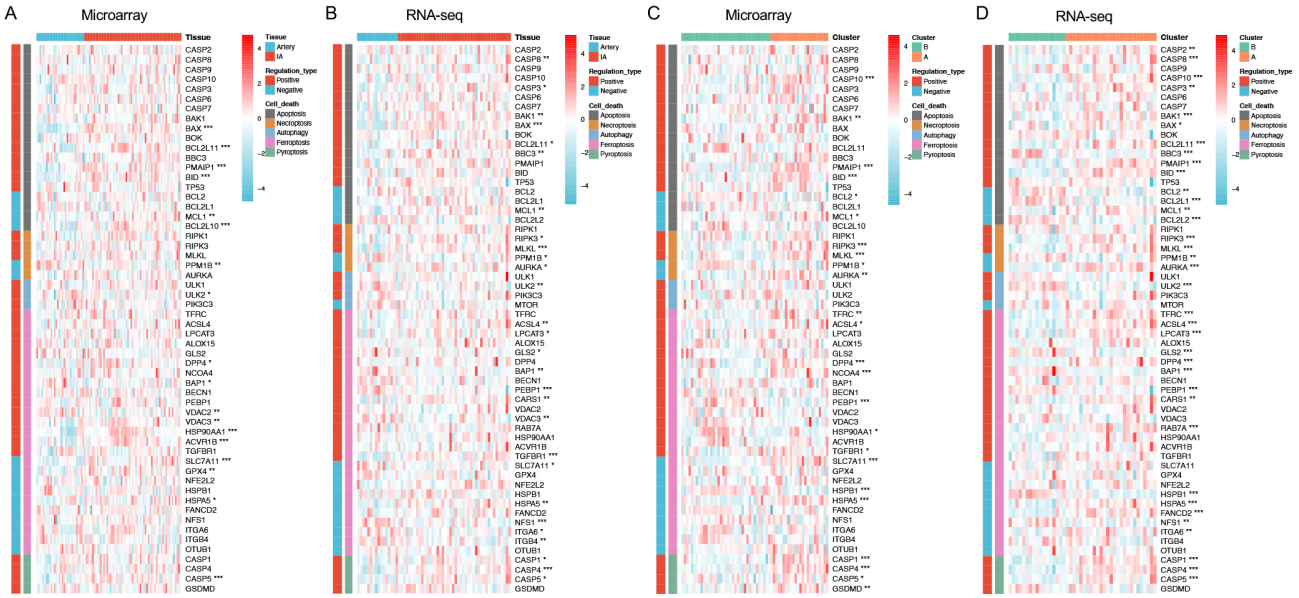

Fig. 3. Expression of cell death-related regulators. (A,B) Heatmaps visualizing the differential expression levels of cell death-related regulators between IA and control tissues. (C,D) Heatmaps visualizing the differential expression levels of cell death-regulators between the two cell death clusters. $*p < 0.05$, $**p < 0.01$, $***p < 0.001$.

hub genes identified by CytoHubba plugin using the degree algorithm were EGFR, CXCR4, CTSB, FASLG, TIMP1, GZMB, NLRP3, CCR2, CD69 and CD2 (Fig. 4E).

3.4 A Novel Cell Death Classification for IAs

Consensus clustering analysis was used to determine the potential integrative cell death classification of IAs. According to the relative change in the area under the CDF curve and the consensus heatmap, the optimal number of clusters was determined to be two. All patients in the microarray dataset were divided into two cell death clusters, with no appreciable increase detected in the area under the CDF curve (Fig. 5A–C). A similar result was also obtained with the RNA-seq dataset (Fig. 5G–I). PCA showed the cell death signature could separate IAs into two distinguishable patterns (Fig. 5D,J). Based on the cell death signature ssGSEA scores, cluster A could be defined as a cell death-high subtype, and cluster B as a cell death-low subtype (Fig. 5E,K). Furthermore, the cell death-based classification was associated with different clinical phenotypes: cluster A had a high risk of rupture, but cluster B had a relatively lower rate of rupture (Fig. 5F,L). A consensus clustering analysis was also performed to identify potential IA subtypes based on different types of cell death. Apoptosis-, necroptosis-, autophagy-, ferroptosis- and pyroptosis-based clustering separated the IAs into two similar clusters. Overall, the Sankey diagrams indicated the cell death signature-based classification provided a better reflection of the clinical phenotypes than the clusters established for each independent type of cell death (**Supplementary Fig. 4**).

3.5 DEGs and Pathway Enrichment Between Different Cell Death Subtypes

Given that patients in cluster A had a high risk of rupture, we further investigated DEGs and functional pathways between the two cell death clusters so as to better understand the potential mechanism of IA progression. DEGs between the two clusters are shown in Fig. 6A,B and Fig. 6E,F. GO and KEGG enrichment analysis revealed the DEGs were significantly enriched in immune-related terms (e.g., lymphocyte activation, mononuclear cell proliferation, macrophage activation, and mast cell activation). Furthermore, inflammatory pathways (e.g., cytokine activity and chemokine signaling pathway), ECM degradation-related processes (e.g., extracellular matrix disassembly and collagen catabolic process) were activated, but smooth muscle contraction and muscle tissue development were significantly inhibited (z-score <0) in cluster A (**Supplementary Fig. 5C–H**).

GSVA revealed that patients in cluster A showed upregulation of cell growth and death-related pathways including apoptosis, ferroptosis, necroptosis and pyroptosis, as well as signal transduction pathways such as MAPK, VEGF, JAK-STAT, NF-κB, TNF and HIF-1. Cluster B showed marked upregulation of Hedgehog, TGF-β and Hippo signaling pathways. Samples in cluster A were also significantly enriched in various immune system-related pathways (Fig. 6C,G). Spearman correlation analysis showed that activation of apoptosis, necroptosis, ferroptosis and pyroptosis were strongly and positively correlated with the activation of VEGF, JAK-STAT, NF-κB, TNF, Toll-like receptor, NOD-like receptor and chemokine signaling pathways. Furthermore, the expression of mTOR

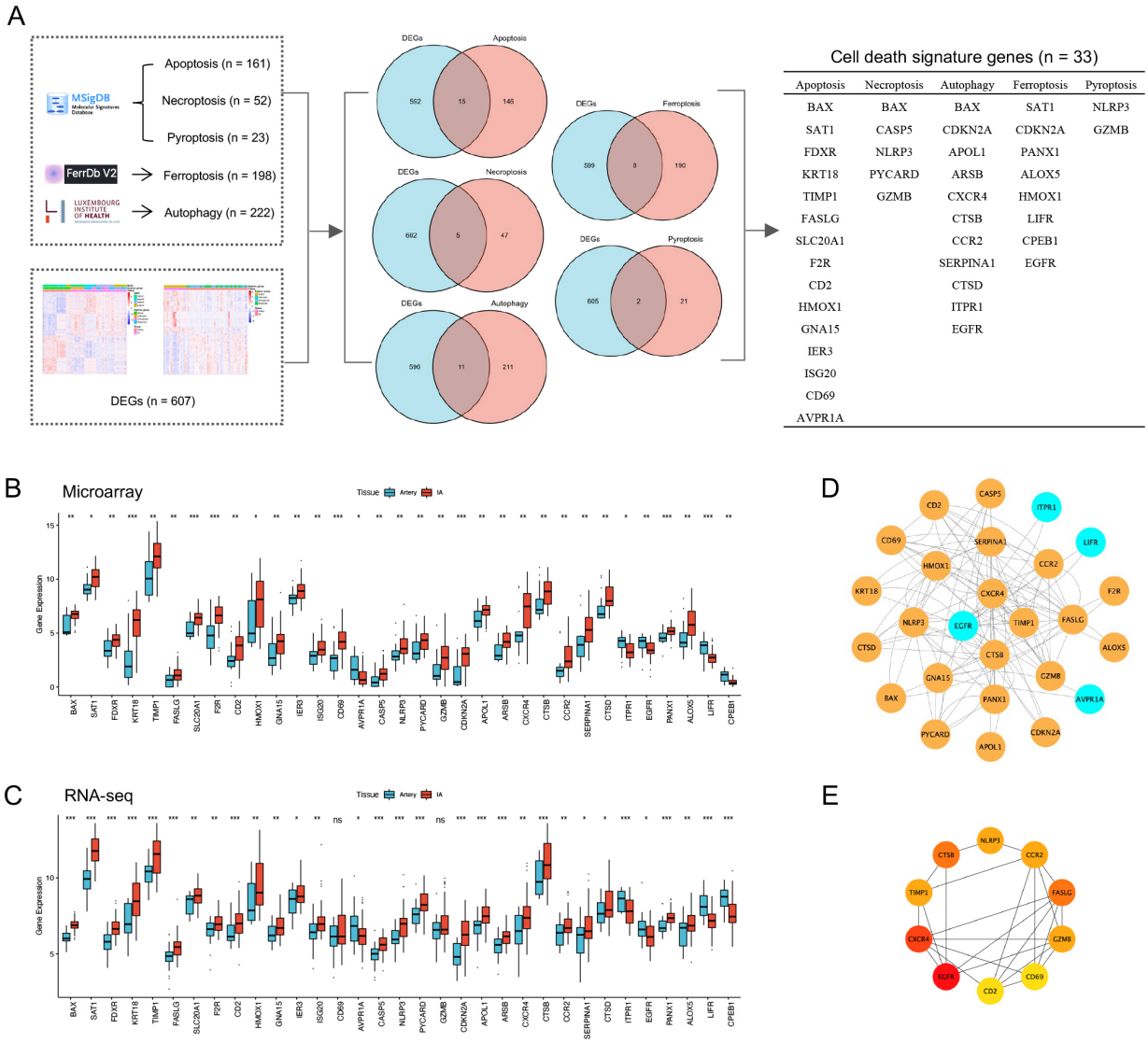

Fig. 4. Identification of cell death signature genes. (A) Venn diagram of various cell death-related genes and DEGs. Table showing cell death signature genes. (B,C) Boxplots of cell death signature genes in IAs compared to control tissues. (D) The PPI network of cell death signature genes. Orange represents upregulated DEGs, while blue represents downregulated DEGs. (E) Construction of PPI network for the top 10 cell death signature genes; the redder the color, the higher the rank. ns $p \geq 0.05$, *$p < 0.05$, **$p < 0.01$, ***$p < 0.001$.

signaling pathways was significantly and positively correlated with the activation of autophagy (Fig. 6D,H).

Cluster A also showed overexpression of multiple apoptosis-positive regulators (e.g., CASPs, BAK1, BAX, BCL2L11, PMAIP1, BBC3, BID), necroptosis-positive regulators (RIPK3 and MLKL), autophagy-positive regulator (ULK2), ferroptosis-positive regulators (e.g., TFRC, ACSL4, LPCAT3, DPP4, NCOA4 and CARS1) and pyroptosis-positive regulators (e.g., CASP1, CASP4, CASP5 and GSDMD), but low expression of apoptosis-negative regulators (e.g., BCL2, BCL22L1, MCL1 and BCL2L2), necroptosis-negative regulator (PPM1B) and ferroptosis-negative regulators (e.g., HSPB1 and NFS1) (Fig. 3C,D). The simultaneous upregulation of multiple positive regulators and downregulation of negative regulators indicated that various cell death processes were activated in cluster A.

3.6 Immune Differences Between the Two Cell Death Clusters

Differences in immune cell infiltration between the two cell death patterns was also investigated. In general, IA tissues in cluster A had higher immune scores and microenvironment scores than those in cluster B. MCPcounter analysis revealed that IA samples in cluster A had significantly higher levels of T cells, cytotoxic lymphocytes, B lineage cells, NK cells, monocytic lineage cells, and myeloid dendritic cells. xCell analysis also showed that IAs

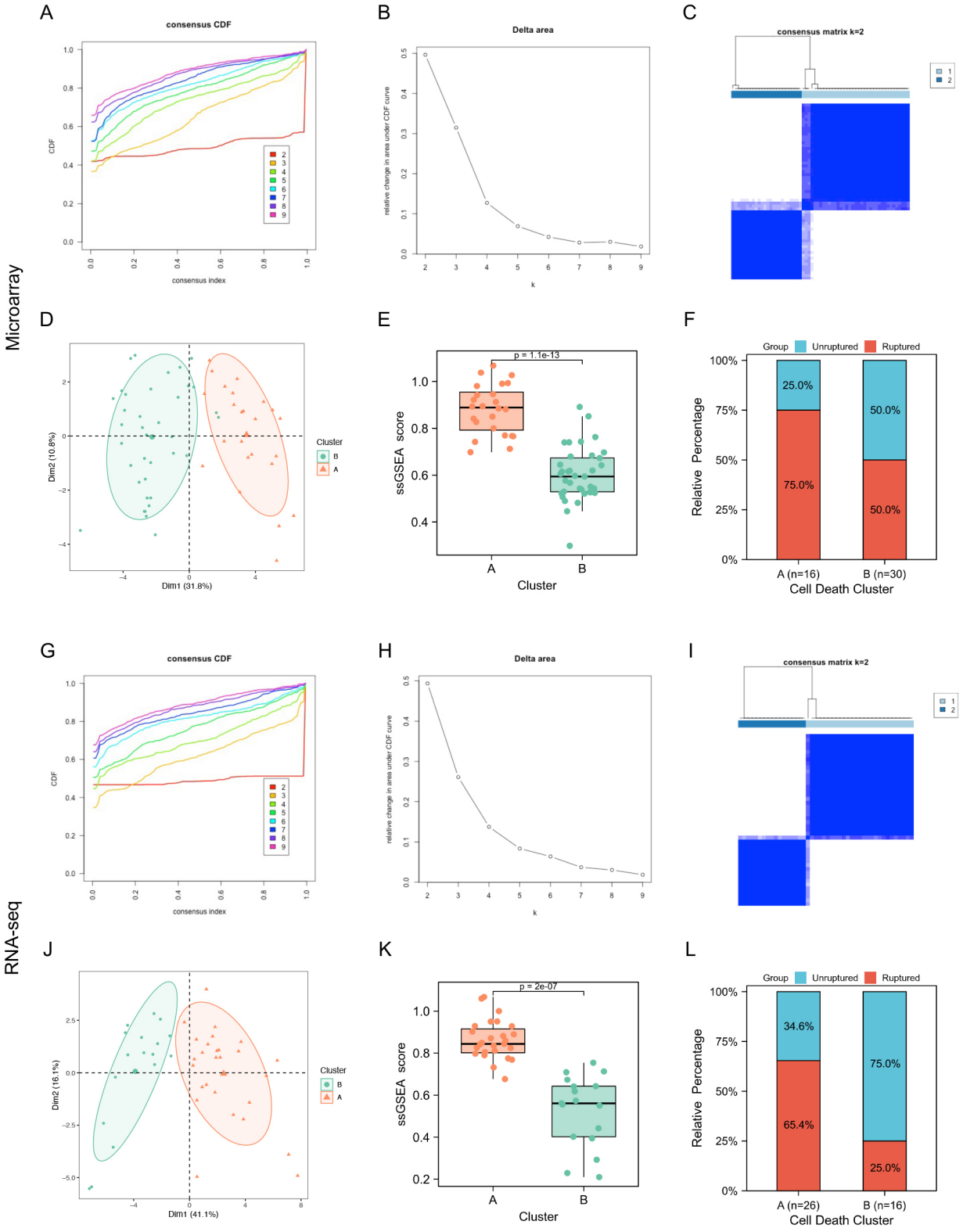

Fig. 5. Novel cell death classification of intracranial aneurysms (IAs) determined from the microarray set (A–F) and from the RNA-seq set (G–I). (A,G) Cumulative distribution function (CDF) curves of the consensus score (k = 2–9). (B,H) Relative change in the area under the CDF curve (k = 2–9). (C,I) Consensus clustering matrix for k = 2, which was the optimal number of clusters. (D,J) Principal component analysis (PCA) according to cell death clusters. (E,K) Boxplots of single sample GSEA (ssGSEA) scores of IA samples in cluster A compared to cluster B. (F,L) Distribution of different rupture status groups within cell death clusters.

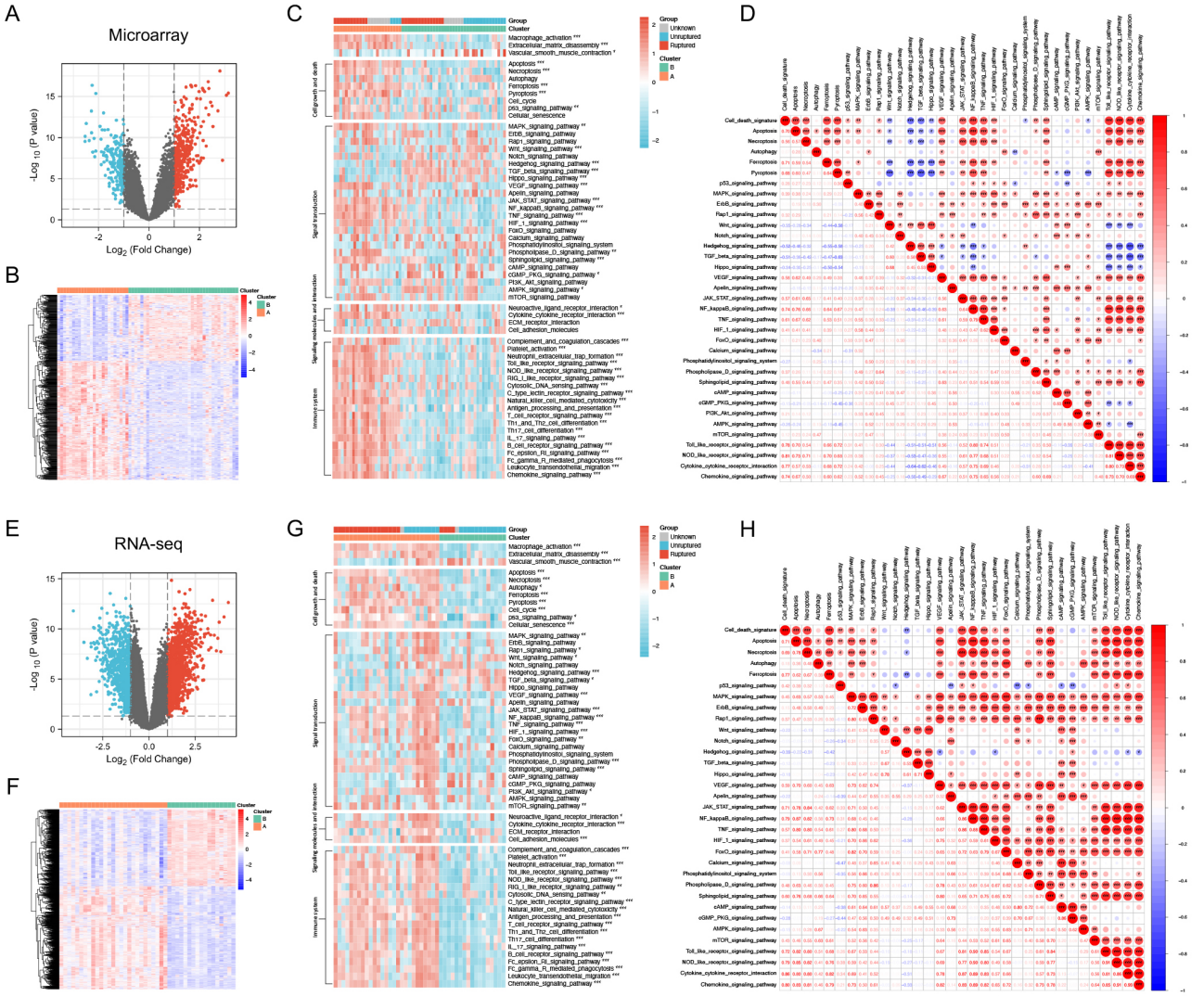

Fig. 6. Subgroup analysis between the two cell death clusters in the microarray (A–D) and RNA-seq sets (E–H). Volcano plots (A,E) and heatmaps (B,F) of DEGs between the two cell death clusters. (C,G) Heatmaps visualizing the GSVA results of cell death, signal transduction, and immune system-related pathways between the different cell death clusters. (D,H) Spearman correlation analysis of the GSVA scores for these pathways in IAs. $*p < 0.05$, $**p < 0.01$, $***p < 0.001$.

in cluster A had more infiltration of dendritic cells (DCs), mast cells, monocytes, macrophages and B cells (Fig. 7A). In addition, the infiltration levels of macrophages, M1 macrophages, mast cells, T cells and B cells were positively correlated with the cell death scores of IA samples (Fig. 7B). Similar results were observed with the RNA-seq dataset (Fig. 7C,D).

We further analyzed correlations between the GSVA scores of different RCD and the degree of immune cell infiltration in all IA samples (**Supplementary Fig. 6**). This analysis showed that activation of apoptosis, necroptosis, ferroptosis and pyroptosis in IAs was positively correlated with the degree of infiltration by monocytes, macrophages, T cells and B cells. Interestingly, activation of the above types of RCD was significantly and positively correlated with the expression of M1 macrophages. However, the activation of M2 macrophages was positively correlated with activation of autophagy, indicating that autophagy plays an opposite role to other types of RCD in the regulation of macrophage phenotype switching.

3.7 WGNCA and PPI Network

The optimal soft threshold values in the microarray and RNA-seq cohorts were 3 and 6, respectively (Fig. 8A and **Supplementary Fig. 7A**). Fig. 8B and **Supplementary Fig. 7B** show the results of gene clustering and recognition of co-expression modules. In the microarray set, the turquoise module correlated significantly with cluster A ($r = 0.86$, $p < 0.001$), while the blue module was significantly related to cluster B ($r = 0.45$, $p < 0.001$) (Fig. 8C). In the RNA-seq cohort, the green/yellow module was significantly associated with cluster A (r = 0.74,

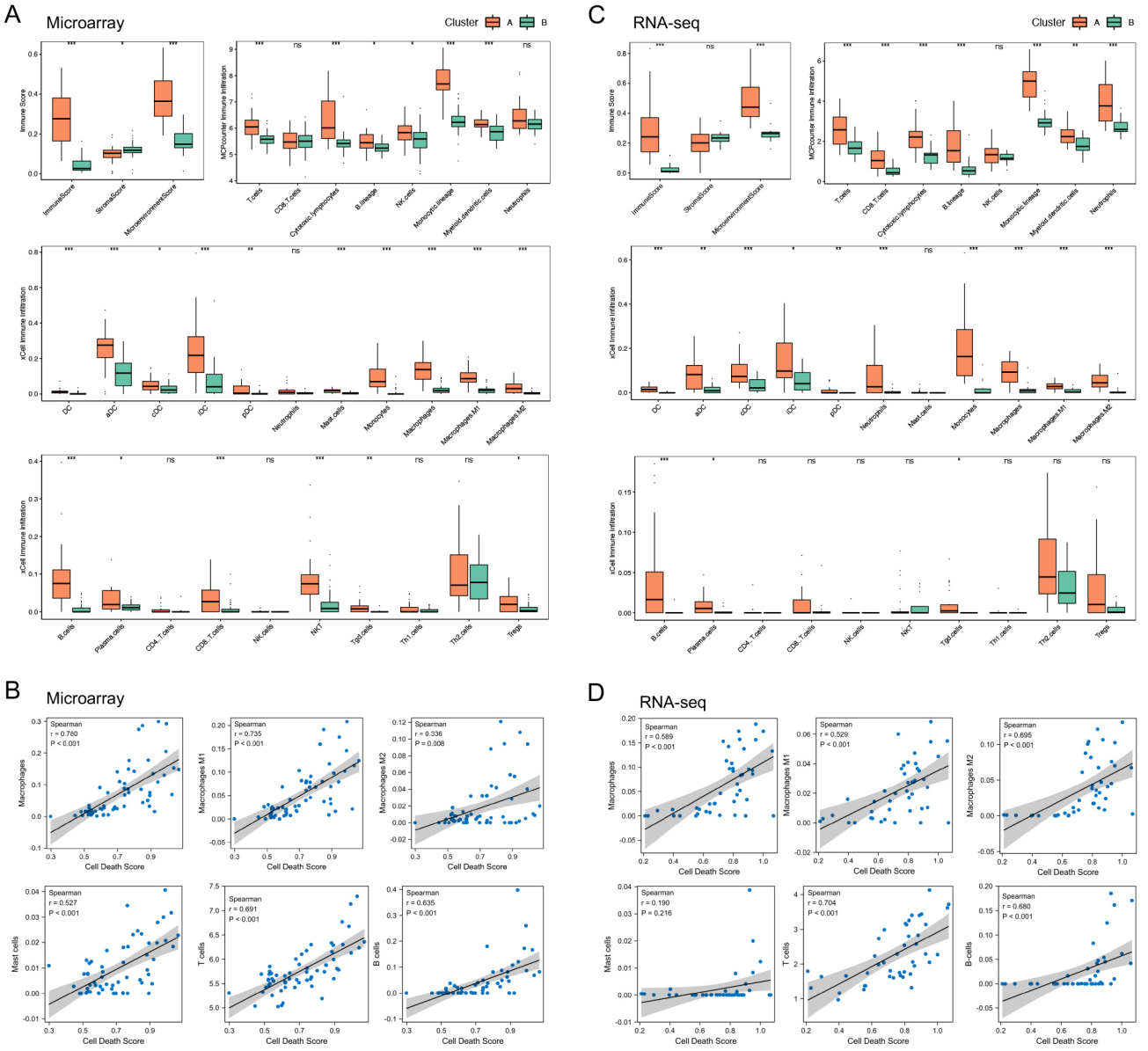

Fig. 7. Immune characteristics of the two cell death clusters. (A,C) Immune cell content histogram. (B,D) Spearman correlation analysis between cell death scores and the infiltration levels of immune cells. ns $p \geq 0.05$, *$p < 0.05$, **$p < 0.01$, ***$p < 0.001$.

$p < 0.001$), and the cyan module to cluster B (r = 0.85, $p < 0.001$) (**Supplementary Fig. 7C**). The genes within the modules were significantly correlated with the traits (cluster A and cluster B) (Fig. 8D,E and **Supplementary Fig. 7D,E**). The genes in the turquoise module were uploaded to the STRING database and the degree scores of each protein calculated by Cytoscape using the CytoHubba plugin. The PPI network found the core proteins related to cluster A were CD4, TYROBP, ITGB2, CD8A, SYK, IL10, TLR2, CD86, CCR5, CDF1R, LYN, LCP2, CD44, VAV1 and CD28 (Fig. 8F). A similar PPI network was obtained from the green/yellow module in the RNA-seq cohort (**Supplementary Fig. 7F**).

3.8 Construction and Validation of a Prediction Model for IA Rupture

Since IAs in cell death cluster A had a relatively higher risk of rupture, DEGs between cell death cluster A and B were used to identify predictive variables for rupture. Following the removal of samples with unclear rupture status, 46 cases were obtained from the microarray dataset (as the training cohort) and 42 from the RNA-seq dataset (as the validation cohort). LASSO regression in the training cohort retained 23 genes (Fig. 9A,B). In addition, the top 20 genes according to the mean decrease Gini by RF were also selected as candidate variables (Fig. 9C,D). Seven genes were thus identified by intersecting the candidate genes obtained by the LASSO and RF algorithms (Fig. 9E). Subsequently, univariate regression identified ANPEP, STK10,

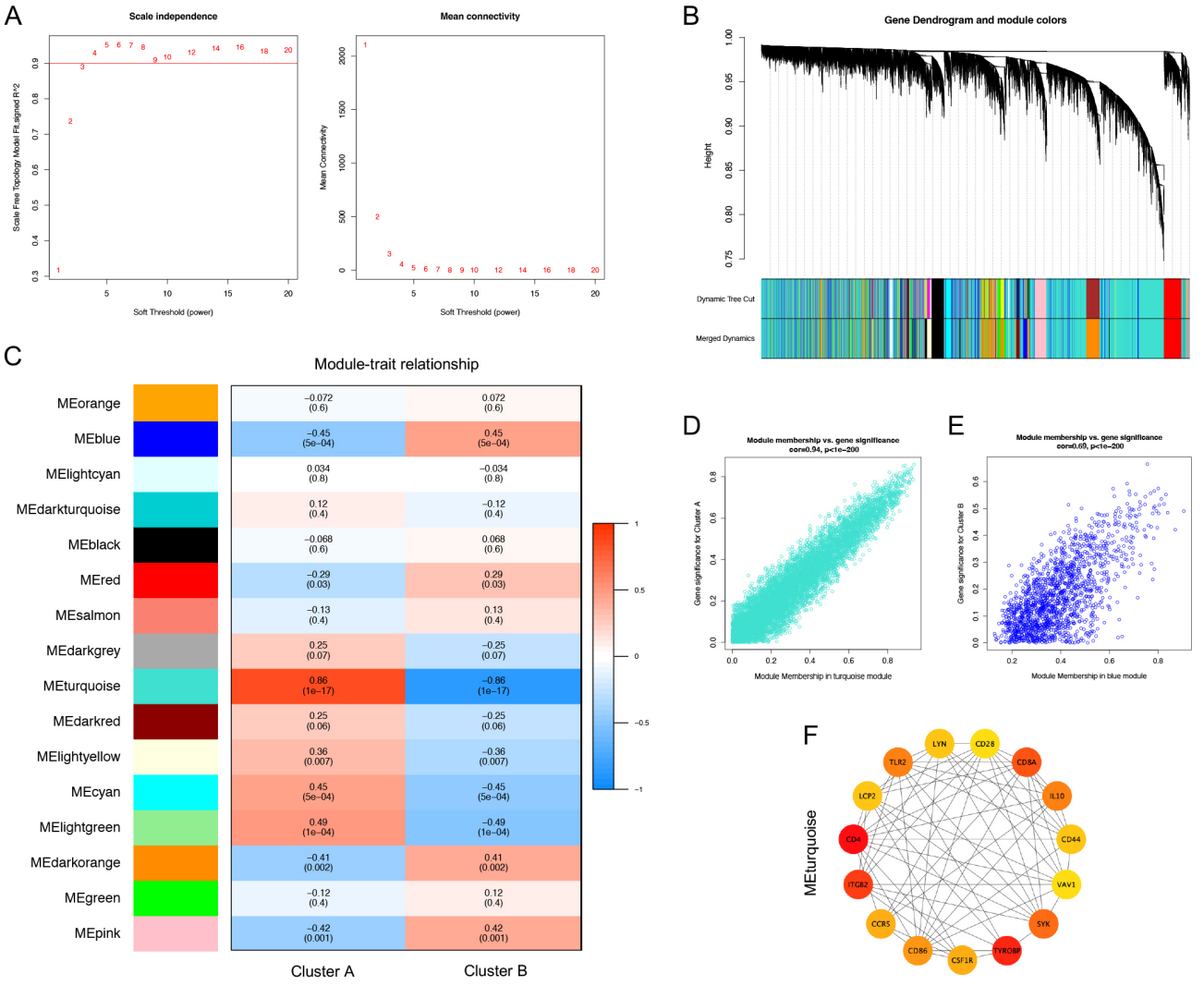

Fig. 8. Weighted gene co-expression network analysis (WGCNA) in the microarray cohort. (A) Scale-free fit index and mean connectivity for different soft powers (optimal soft threshold $\beta = 3$). (B) Gene clustering and recognition of co-expression modules. (C) Heatmap of the correlations between gene modules and cell death clusters. (D,E) Correlation between traits (cluster A and cluster B) and genes in the modules. (F) Construction of the PPI network of hub genes in the turquoise module: the redder the color, the higher the rank.

DSC2, HPSE, IGFBP1, and S100A8 as risk factors for IA rupture, each with an odds ratio (OR) >1 and a $p < 0.05$ (Fig. 9F). ROC curve analysis revealed the efficacy of these 6 genes for independently predicting IA rupture (Fig. 9G). Boxplots showed that all of them were upregulated in ruptured IAs (Fig. 9H). Finally, a prediction model was constructed based on the 6 characteristic genes and using a multifactor, generalized linear model: Y = (–37.5607) + (1.3321) × ANPEP + (–0.694) × STK10 + (0.6081) × DSC2 + (1.93) × HPSE + (1.4639) × IGFBP1 + (0.7208) × S100A8. The model demonstrated good accuracy in estimating the risk of rupture, with a C index of 0.92 (95% CI, 0.85–1.00) and an area under curve (AUC) of 0.924 in the training cohort (Fig. 9I). The p value of the HL test was 0.841 (>0.05) and the calibration curve was close to 45°, indicating a well-calibrated model (Fig. 9J). In the validation cohort, the predictive model displayed a C index of 0.85 (95% CI, 0.74–0.97) and an AUC of 0.855 for the prediction of IA rupture. The calibration plot also showed accurate predictive ability in the validation cohort (**Supplementary Fig. 8**).

4. Discussion

The current study is the first to our knowledge to investigate the role of various types of cell death in the formation and progression of IA. A novel classification system was developed that separated IAs into two cell death clusters, each with different mechanisms. Furthermore, a prediction model for IA rupture based on the DEGs identified between the two clusters was established and validated.

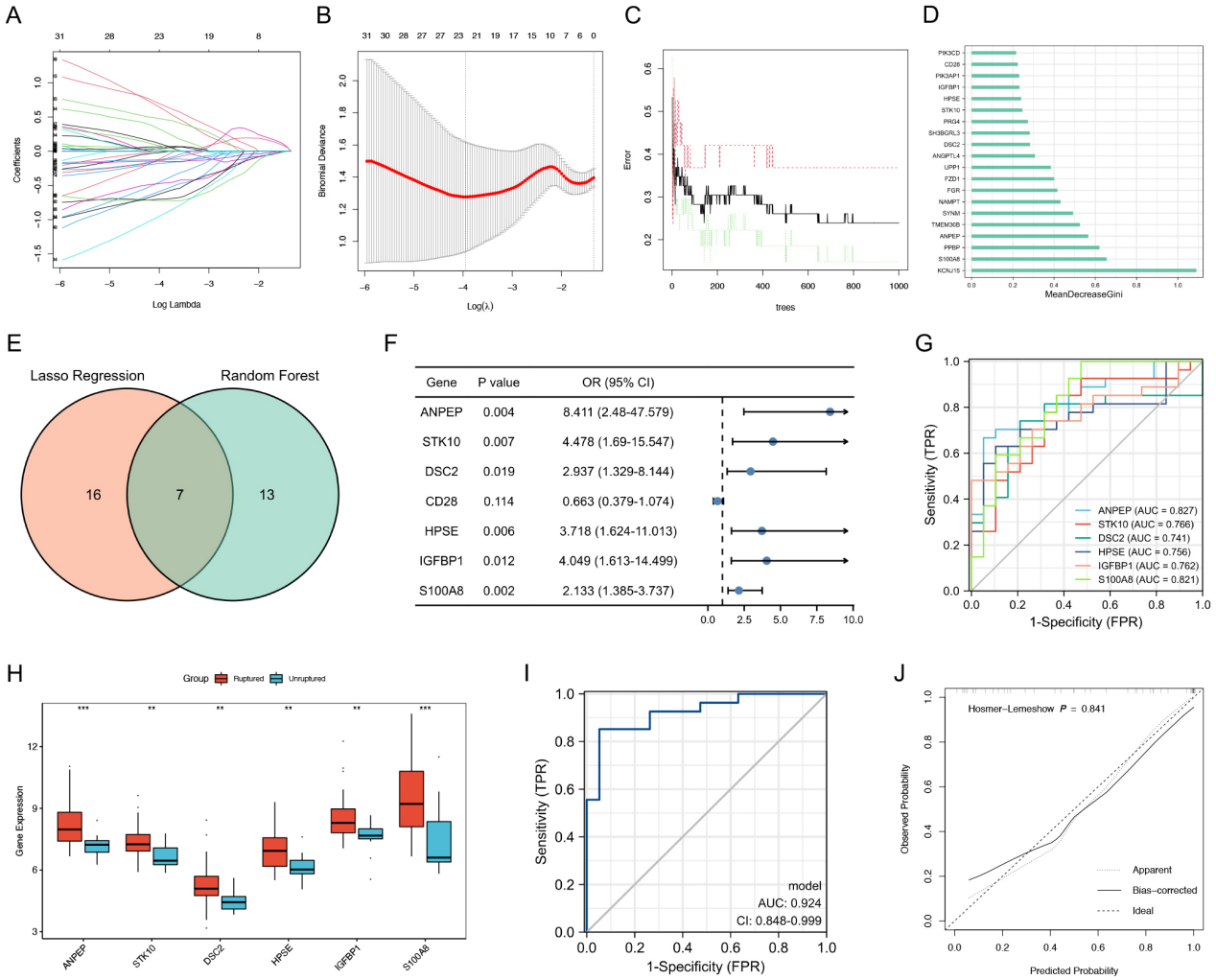

Fig. 9. Construction of the prediction model for IA rupture in the training cohort. (A) Screening of candidate genes using the LASSO algorithm. (B) Cross-validation for tuning parameter screening in the LASSO regression model. (C) Correlation plot between the number of trees in random forest (RF) and the model error. (D) The mean decrease in Gini index of the top 20 genes calculated in the RF classifier. (E) Venn diagram of candidate genes obtained from LASSO and RF. (F) Univariate logistic regression analysis of the seven candidate genes, which yielded six genes linked to rupture. (G) ROC curve and AUC values of the six risk genes for the prediction of rupture. (H) Boxplots of six risk genes in ruptured IAs compared to unruptured IAs. (I) ROC curve and AUC values of the prediction model in rupture prediction. (J) Calibration plot of the prediction model. *$p < 0.05$, **$p < 0.01$, ***$p < 0.001$.

Abnormalities in RCD processes including apoptosis, necroptosis, autophagy, ferroptosis and pyroptosis have been observed in the pathogenesis of various diseases [13, 14]. The first major finding of our study was that multiple types of cell death were found to be associated with IA formation and progression. Apoptosis is a caspase-dependent RCD that can be triggered by intrinsic and extrinsic pathways [13,32]. Intracellular stress such as DNA damage, endoplasmic reticulum stress (ERS), and BH3-only proteins such as BID can initiate the intrinsic pathway by binding the anti-apoptotic protein BCL2, thereby leading to activation of cell death effectors (BAX and BAK) [33]. ERS is an inducer of apoptosis and has been implicated in the formation of IA [34]. In the present study, BID, BAX and multiple CASPs were found to be overexpressed in IAs. Moreover, BCL2 was downregulated in cluster A, indicating involvement of the intrinsic apoptotic pathway in IA formation and progression. Activation of the tumor necrosis factor (TNF) receptor family member FAS and its ligand FASLG has been shown to trigger the extrinsic apoptotic pathway [35]. Caspase-8-mediated proteolytic activation of BID can connect the intrinsic and extrinsic apoptotic pathways [36]. The observed overexpression of FASLG, BID and CASP8 implies the extrinsic pathway is also activated during IA pathogenesis. Previous studies have reported increased levels of VSMC apoptosis in both human IA and ruptured IA specimens [15–18]. In addition, several factors have been found to induce VSMC apoptosis, including hemodynamic stimulation and inflammation cytokines such as IL-1β and iNOS [37,38].

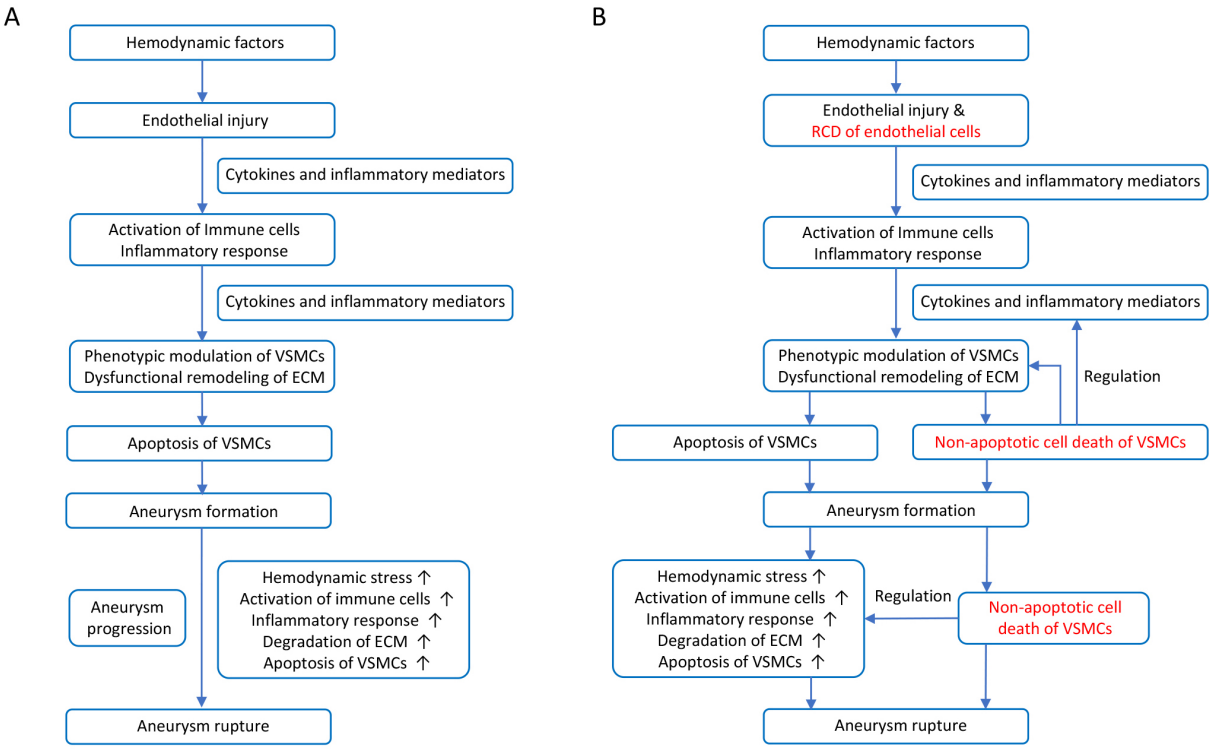

Fig. 10. Mechanism of intracranial aneurysm (IA) formation and rupture. (A) Classical mechanism of IA formation and rupture. (B) Novel mechanism of IA formation and rupture.

Pyroptosis is an inflammatory, lytic type of RCD [39]. In the canonical pyroptotic pathway, cytoplasmic sensors such as NOD-like receptors (NLRPs) can recognize damage-associated molecular patterns (DAMPs) or pathogen-associated molecular patterns (PAMPs), promote the release of pro-inflammatory cytokines, and participate in the assembly of inflammasomes [19,39]. The nucleotide-binding oligomerization domain-like receptor family pyrin domain containing 3 (NLRP3) inflammasome is the most studied inflammasome and is considered to be a critical driver of multiple vascular diseases [40]. In the present study, NLRP3 was found to be overexpressed in IAs compared to controls. Using immunohistochemistry, Zhang *et al.* [41] reported greater expression of the NLRP3 inflammasome in the walls of ruptured human IAs than in unruptured tissues. A recent study also showed that activation of the NLRP3/IL-1β/MMP9 pathway facilitates the rupture of IA in an estrogen-deficient rat model [42]. Therefore, NLRP3 is involved in both IA formation and rupture. MMP9 plays a significant role in ECM remodeling [43]. Thus, we also speculated that pyroptosis is likely to be involved in the formation and progression of IA through inflammation and degradation of the ECM. Furthermore, transcriptional upregulation of pro-IL-1β and NLRP3 is mediated by the NF-κB signaling pathway and is the first stage of the NLRP3 inflammasome event [40]. In the present study, the NF-κB signaling pathway was significantly enriched in the cell death-high cluster. *In vitro* and *in vivo* experiments have also shown this pathway is involved in the pathogenesis of IA [44–46]. Moreover, gasdermin D (GSDMD), a member of the gasdermin superfamily, is the key executor of pyroptosis and is cleaved by CASP1/4/5/11 [14,19,39]. These molecules were also found in the current study to be overexpressed in the cell death-high cluster. Furthermore, Liu *et al.* [47] demonstrated that serum IL-1β and pyroptosis-related proteins were correlated with aneurysm wall enhancement in unruptured IA, suggesting that pyroptosis may be associated with the progression of IA. Together, the above evidence indicates that pyroptosis may be involved in the pathogenesis of IA.

Necroptosis is a lytic form of RCD [48]. The necroptotic process involves the autophosphorylation of receptor-interacting protein kinase 1 (RIPK1) which in turn activates RIPK3 kinase and then RIPK3-mediated phosphorylation of mixed-lineage kinase domain-like protein (MLKL), leading to membrane lysis [49–51]. Human vascular diseases such as ischemic stroke, myocardial infarction and aortic aneurysm (AA) are closely associated with necroptosis [52]. Wang *et al.* [53] reported elevated levels of RIPK3 and RIPK1 in human AA. They also found that SMC necroptosis can be triggered by RIPK3, and that lack of RIPK3 prevents the formation of AA in mice. Subsequent research also showed that RIPK1 inhibitors can promote tissue repair and reduce inflammation in murine AA induced by elastase [54]. Zhou *et al.* [55] found that MLKL and CaMKII were involved in RIPK3-mediated

SMC necroptosis in mouse AA models. In the current study, higher expression levels of RIPK3 and MLKL were found in IAs than in controls, and higher levels in cluster A than in cluster B. In addition, necroptosis can be triggered by multiple stimuli, such as the TNF (tumor necrosis factor) signaling pathway, death receptors (e.g., FAS and FASLG), Toll-like receptors (TLR3 and TLR4), and nucleic acid sensors (e.g., ZBP1) [19,56]. Our study revealed the TNF and Toll-like receptor signaling pathways were strongly correlated with necroptosis, potentially indicating they share a regulatory relationship. Therefore, we speculate that necroptosis may play a role in the formation and progression of IA, but further experimental validation is needed.

Ferroptosis is a form of iron-dependent RCD [57]. Iron overload and accumulation of lipid peroxide are the two characteristic features of ferroptosis [57]. Iron deposition is the key trigger for ferroptosis and is elevated in IA tissues compared to controls [58]. Oxidative stress and reactive oxygen species (ROS) have been widely associated with a variety of vascular diseases, including IA, AA, aortic dissection (AD), and atherosclerosis (AS) [59–62]. Increasing evidence suggests that excessive ROS-produced oxidative stress can trigger endothelial damage through ferroptosis and pyroptosis [63]. Furthermore, Sampilvanjil *et al*. [64] showed that the death of VSMC induced by a cigarette smoke extract was ignited by ferroptosis. Zhang *et al*. [65] also demonstrated that ferroptosis induces VSMC phenotypic switching and neointimal hyperplasia in mice. Furthermore, the present study found that several molecular components of ferroptosis were upregulated in IA tissue and in cluster A, including ACSL4 and LPCAT3. A recent study found that ferroptosis is significantly activated in a mouse model with caroid artery injury, and also indicated that activated ferroptotic stress facilitates the dedifferentiation of SMC by modulating mitochondrial function [66]. Jin *et al*. [67] found that the ferroptosis inhibitor ferrostatin-1 blocked the VSMC inflammation induced by high hydrostatic pressure. Overall, the above results indicate that ferroptosis may be related to the pathogenesis of IA.

Autophagy plays an important role in cell survival, bioenergetic homoeostasis, organism development, and in the regulation of cell death [68]. A previous study found that the expression of autophagy-related genes, including LC-3, Beclin-1, ATG5, and ATG14, was significantly higher in IA tissues compared to normal vessel tissues [69]. An *in vitro* study also found that shear stress induces modulation of the VSMC phenotype through autophagy mediated by AMPK/mTOR/ULK1 [70]. SPARC has been shown to induce phenotypic modulation of human brain VSMCs through AMPK/mTOR-mediated autophagy [71], with mTOR being a crucial inhibitor of autophagy [72]. An inhibitor of mTOR, rapamycin, has been shown to suppress IA development and to limit the growth of AA in mouse models [73,74]. Although excessive activation of autophagy can induce autophagic cell death [75], our study found that autophagy was not significantly activated in IA. Therefore, we speculate that normal activation of autophagy may have a protective effect on IA.

Of note, non-apoptotic RCD is closely related to inflammation and immunity [14,19]. Mature IL-1β and IL-18 are released from cells during the pyroptotic process and subsequently cause inflammatory responses [76]. RIPK1 can promote neuroinflammation during the necroptotic process, and this is considered to be a key driver of neurodegeneration [77]. Furthermore, pyroptosis, necroptosis and ferroptosis can all cause membrane rupture, resulting in the release of intracellular components that contain numerous inflammatory mediators [14,19]. However, autophagy has the effect of limiting inflammation [78]. For example, autophagy can clear the sources of DAMPs and ROS, thereby inhibiting the subsequent activation of inflammation and cell death [78]. In addition, a mutual regulatory relationship exists between cell death and immune cells. For example, ferroptosis can be triggered by iron, and ferroptosis-related regulators such as SLC7A11 and GPX4 can regulate cell death in macrophages [79]. In the present study, correlations were observed between various cell death processes and multiple inflammation-related pathways. We also found a correlation between RCD and the infiltration of multiple immune cell types such as monocytes, macrophages, B cells and T cells. Interestingly, our results indicated that apoptosis, necroptosis, ferroptosis and pyroptosis may activate M1 macrophages, but that autophagy may upregulate M2 macrophages. Indeed, macrophage polarization is known to play an important role in aneurysm formation and rupture [80]. M1 macrophages can upregulate the inflammatory process and promote the development of aneurysms [81]. Therefore, regulation of the M1/M2 ratio through the targeting of different types of RCD offers new prospects for IA treatment.

In summary, in addition to directly causing the death of endothelial cells and VSMCs, RCD also has multiple roles in the development of IA, including the modulation of inflammation and immunity (Fig. 10). These novel insights offer new directions for further mechanistic research and treatment of IA.

There were several limitations in this study. One was the lack of basic biological experiments to confirm the role of different RCD in IA pathogenesis. Another was the absence of clinical data such as the size of aneurysms, meaning it was not possible to quantify the relationship between the expression of various RCD components and IA progression.

5. Conclusions

In conclusion, our study found that multiple RCD pathways may be involved in IA formation and rupture, and that these cell death processes were correlated with inflammation and immunity. We also established an inte-

grated classification system based on cell death, as well as a prediction model for IA rupture. Furthermore, we present novel insights into the mechanism of IA pathogenesis that may help to guide future research.

Availability of Data and Materials

The public data could be downloaded at (https://www.ncbi.nlm.nih.gov/geo/).

Author Contributions

JZ and DK designed the research study. JZ, ZW and JL analyzed the data. JZ and ZW wrote the manuscript. All authors contributed to editorial changes in the manuscript. All authors read and approved the final manuscript.

Ethics Approval and Consent to Participate

Not applicable.

Acknowledgment

We thank Ejear English editing service for the language editing in the manuscript.

Funding

This research was funded by the National Nature Science Foundation of China (grant number 82171327), Startup Fund for scientific research, Fujian Medical University (grant number 2022QH2029).

Conflict of Interest

The authors declare no conflict of interest.

Supplementary Material

Supplementary material associated with this article can be found, in the online version, at https://doi.org/10.31083/j.fbl2811289.

References

[1] Vlak MH, Algra A, Brandenburg R, Rinkel GJ. Prevalence of unruptured intracranial aneurysms, with emphasis on sex, age, comorbidity, country, and time period: a systematic review and meta-analysis. The Lancet. Neurology. 2011; 10: 626–636.

[2] Rincon F, Rossenwasser RH, Dumont A. The epidemiology of admissions of nontraumatic subarachnoid hemorrhage in the United States. Neurosurgery. 2013; 73: 217–222; discussion 212–213.

[3] Thompson BG, Brown RD, Jr, Amin-Hanjani S, Broderick JP, Cockroft KM, Connolly ES, Jr, *et al*. Guidelines for the Management of Patients With Unruptured Intracranial Aneurysms: A Guideline for Healthcare Professionals From the American Heart Association/American Stroke Association. Stroke. 2015; 46: 2368–2400.

[4] Hasan DM, Mahaney KB, Brown RD, Jr, Meissner I, Piepgras DG, Huston J, *et al*. Aspirin as a promising agent for decreasing incidence of cerebral aneurysm rupture. Stroke. 2011; 42: 3156–3162.

[5] Makino H, Tada Y, Wada K, Liang EI, Chang M, Mobashery S, *et al*. Pharmacological stabilization of intracranial aneurysms in mice: a feasibility study. Stroke. 2012; 43: 2450–2456.

[6] Shimada K, Furukawa H, Wada K, Korai M, Wei Y, Tada Y, *et al*. Protective Role of Peroxisome Proliferator-Activated Receptor-γ in the Development of Intracranial Aneurysm Rupture. Stroke. 2015; 46: 1664–1672.

[7] Liu Z, Ajimu K, Yalikun N, Zheng Y, Xu F. Potential Therapeutic Strategies for Intracranial Aneurysms Targeting Aneurysm Pathogenesis. Frontiers in Neuroscience. 2019; 13: 1238.

[8] Miyata T, Minami M, Kataoka H, Hayashi K, Ikedo T, Yang T, *et al*. Osteoprotegerin Prevents Intracranial Aneurysm Progression by Promoting Collagen Biosynthesis and Vascular Smooth Muscle Cell Proliferation. Journal of the American Heart Association. 2020; 9: e015731.

[9] Kataoka H. Molecular mechanisms of the formation and progression of intracranial aneurysms. Neurologia Medico-chirurgica. 2015; 55: 214–229.

[10] Signorelli F, Sela S, Gesualdo L, Chevrel S, Tollet F, Pailler-Mattei C, *et al*. Hemodynamic Stress, Inflammation, and Intracranial Aneurysm Development and Rupture: A Systematic Review. World Neurosurgery. 2018; 115: 234–244.

[11] Frösen J, Cebral J, Robertson AM, Aoki T. Flow-induced, inflammation-mediated arterial wall remodeling in the formation and progression of intracranial aneurysms. Neurosurgical Focus. 2019; 47: E21.

[12] Texakalidis P, Sweid A, Mouchtouris N, Peterson EC, Sioka C, Rangel-Castilla L, *et al*. Aneurysm Formation, Growth, and Rupture: The Biology and Physics of Cerebral Aneurysms. World Neurosurgery. 2019; 130: 277–284.

[13] Moujalled D, Strasser A, Liddell JR. Molecular mechanisms of cell death in neurological diseases. Cell Death and Differentiation. 2021; 28: 2029–2044.

[14] Gao W, Wang X, Zhou Y, Wang X, Yu Y. Autophagy, ferroptosis, pyroptosis, and necroptosis in tumor immunotherapy. Signal Transduction and Targeted Therapy. 2022; 7: 196.

[15] Sakaki T, Kohmura E, Kishiguchi T, Yuguchi T, Yamashita T, Hayakawa T. Loss and apoptosis of smooth muscle cells in intracranial aneurysms. Studies with in situ DNA end labeling and antibody against single-stranded DNA. Acta Neurochirurgica. 1997; 139: 469–475.

[16] Kondo S, Hashimoto N, Kikuchi H, Hazama F, Nagata I, Kataoka H. Apoptosis of medial smooth muscle cells in the development of saccular cerebral aneurysms in rats. Stroke. 1998; 29: 181–188; discussion 189.

[17] Pentimalli L, Modesti A, Vignati A, Marchese E, Albanese A, Di Rocco F, *et al*. Role of apoptosis in intracranial aneurysm rupture. Journal of Neurosurgery. 2004; 101: 1018–1025.

[18] Guo F, Li Z, Song L, Han T, Feng Q, Guo Y, *et al*. Increased apoptosis and cysteinyl aspartate specific protease-3 gene expression in human intracranial aneurysm. Journal of Clinical Neuroscience. 2007; 14: 550–555.

[19] Tang D, Kang R, Berghe TV, Vandenabeele P, Kroemer G. The molecular machinery of regulated cell death. Cell Research. 2019; 29: 347–364.

[20] Leek JT, Johnson WE, Parker HS, Jaffe AE, Storey JD. The sva package for removing batch effects and other unwanted variation in high-throughput experiments. Bioinformatics. 2012; 28: 882–883.

[21] Ritchie ME, Phipson B, Wu D, Hu Y, Law CW, Shi W, *et al*. limma powers differential expression analyses for RNA-sequencing and microarray studies. Nucleic Acids Research. 2015; 43: e47.

[22] Subramanian A, Tamayo P, Mootha VK, Mukherjee S, Ebert BL, Gillette MA, *et al*. Gene set enrichment analysis: a knowledge-based approach for interpreting genome-wide expression profiles. Proceedings of the National Academy of Sciences of the United States of America. 2005; 102: 15545–15550.

[23] Hänzelmann S, Castelo R, Guinney J. GSVA: gene set variation analysis for microarray and RNA-seq data. BMC Bioinformatics. 2013; 14: 7.
[24] Luo W, Brouwer C. Pathview: an R/Bioconductor package for pathway-based data integration and visualization. Bioinformatics. 2013; 29: 1830–1831.
[25] Wilkerson MD, Hayes DN. ConsensusClusterPlus: a class discovery tool with confidence assessments and item tracking. Bioinformatics. 2010; 26: 1572–1573.
[26] Wu T, Hu E, Xu S, Chen M, Guo P, Dai Z, *et al*. clusterProfiler 4.0: A universal enrichment tool for interpreting omics data. Innovation. 2021; 2: 100141.
[27] Becht E, Giraldo NA, Lacroix L, Buttard B, Elarouci N, Petitprez F, *et al*. Estimating the population abundance of tissue-infiltrating immune and stromal cell populations using gene expression. Genome Biology. 2016; 17: 218.
[28] Aran D, Hu Z, Butte AJ. xCell: digitally portraying the tissue cellular heterogeneity landscape. Genome Biology. 2017; 18: 220.
[29] Langfelder P, Horvath S. WGCNA: an R package for weighted correlation network analysis. BMC Bioinformatics. 2008; 9: 559.
[30] Harrell FE, Jr, Califf RM, Pryor DB, Lee KL, Rosati RA. Evaluating the yield of medical tests. The Journal of the American Medical Association. 1982; 247: 2543–2546.
[31] Steyerberg EW, Vergouwe Y. Towards better clinical prediction models: seven steps for development and an ABCD for validation. European Heart Journal. 2014; 35: 1925–1931.
[32] Erekat NS. Programmed cell death in cerebellar Purkinje neurons. Journal of Integrative Neuroscience. 2022; 21: 30.
[33] Wang X. The expanding role of mitochondria in apoptosis. Genes & Development. 2001; 15: 2922–2933.
[34] Chen B, Zhou H, Zhou X, Yang L, Xiong Y, Zhang L. Comprehensive Analysis of Endoplasmic Reticulum Stress in Intracranial Aneurysm. Frontiers in Cellular Neuroscience. 2022; 16: 865005.
[35] Krammer PH. CD95's deadly mission in the immune system. Nature. 2000; 407: 789–795.
[36] Strasser A, Jost PJ, Nagata S. The many roles of FAS receptor signaling in the immune system. Immunity. 2009; 30: 180–192.
[37] Sadamasa N, Nozaki K, Hashimoto N. Disruption of gene for inducible nitric oxide synthase reduces progression of cerebral aneurysms. Stroke. 2003; 34: 2980–2984.
[38] Moriwaki T, Takagi Y, Sadamasa N, Aoki T, Nozaki K, Hashimoto N. Impaired progression of cerebral aneurysms in interleukin-1beta-deficient mice. Stroke. 2006; 37: 900–905.
[39] Yu P, Zhang X, Liu N, Tang L, Peng C, Chen X. Pyroptosis: mechanisms and diseases. Signal Transduction and Targeted Therapy. 2021; 6: 128.
[40] Takahashi M. NLRP3 inflammasome as a key driver of vascular disease. Cardiovascular Research. 2022; 118: 372–385.
[41] Zhang D, Yan H, Hu Y, Zhuang Z, Yu Z, Hang C. Increased Expression of NLRP3 Inflammasome in Wall of Ruptured and Unruptured Human Cerebral Aneurysms: Preliminary Results. Journal of Stroke and Cerebrovascular Diseases. 2015; 24: 972–979.
[42] Yamaguchi T, Miyamoto T, Shikata E, Yamaguchi I, Shimada K, Yagi K, *et al*. Activation of the NLRP3/IL-1β/MMP-9 pathway and intracranial aneurysm rupture associated with the depletion of ERα and Sirt1 in oophorectomized rats. Journal of Neurosurgery. 2022; 138: 191–198.
[43] Zhang X, Ares WJ, Taussky P, Ducruet AF, Grandhi R. Role of matrix metalloproteinases in the pathogenesis of intracranial aneurysms. Neurosurgical Focus. 2019; 47: E4.
[44] Baeriswyl DC, Prionisti I, Peach T, Tsolkas G, Chooi KY, Vardakis J, *et al*. Disturbed flow induces a sustained, stochastic NF-κB activation which may support intracranial aneurysm growth in vivo. Scientific Reports. 2019; 9: 4738.
[45] Lai XL, Deng ZF, Zhu XG, Chen ZH. *Apc* gene suppresses intracranial aneurysm formation and rupture through inhibiting the NF-κB signaling pathway mediated inflammatory response. Bioscience Reports. 2019; 39: BSR20181909.
[46] Zhang X, Wan Y, Feng J, Li M, Jiang Z. Involvement of TLR2/4 MyD88 NF κB signaling pathway in the pathogenesis of intracranial aneurysm. Molecular Medicine Reports. 2021; 23: 230.
[47] Liu Q, Zhang Y, Zhu C, Liu W, Ma X, Chen J, *et al*. Serum IL-1, Pyroptosis and Intracranial Aneurysm Wall Enhancement: Analysis Integrating Radiology, Serum Cytokines and Histology. Frontiers in Cardiovascular Medicine. 2022; 9: 818789.
[48] Frank D, Vince JE. Pyroptosis versus necroptosis: similarities, differences, and crosstalk. Cell Death and Differentiation. 2019; 26: 99–114.
[49] Sun L, Wang H, Wang Z, He S, Chen S, Liao D, *et al*. Mixed lineage kinase domain-like protein mediates necrosis signaling downstream of RIP3 kinase. Cell. 2012; 148: 213–227.
[50] Murphy JM, Czabotar PE, Hildebrand JM, Lucet IS, Zhang JG, Alvarez-Diaz S, *et al*. The pseudokinase MLKL mediates necroptosis via a molecular switch mechanism. Immunity. 2013; 39: 443–453.
[51] Laurien L, Nagata M, Schünke H, Delanghe T, Wiederstein JL, Kumari S, *et al*. Autophosphorylation at serine 166 regulates RIP kinase 1-mediated cell death and inflammation. Nature Communications. 2020; 11: 1747.
[52] Khoury MK, Gupta K, Franco SR, Liu B. Necroptosis in the Pathophysiology of Disease. The American Journal of Pathology. 2020; 190: 272–285.
[53] Wang Q, Liu Z, Ren J, Morgan S, Assa C, Liu B. Receptor-interacting protein kinase 3 contributes to abdominal aortic aneurysms via smooth muscle cell necrosis and inflammation. Circulation Research. 2015; 116: 600–611.
[54] Wang Q, Zhou T, Liu Z, Ren J, Phan N, Gupta K, *et al*. Inhibition of Receptor-Interacting Protein Kinase 1 with Necrostatin-1s ameliorates disease progression in elastase-induced mouse abdominal aortic aneurysm model. Scientific Reports. 2017; 7: 42159.
[55] Zhou T, DeRoo E, Yang H, Stranz A, Wang Q, Ginnan R, *et al*. MLKL and CaMKII Are Involved in RIPK3-Mediated Smooth Muscle Cell Necroptosis. Cells. 2021; 10: 2397.
[56] Seo J, Nam YW, Kim S, Oh DB, Song J. Necroptosis molecular mechanisms: Recent findings regarding novel necroptosis regulators. Experimental & Molecular Medicine. 2021; 53: 1007–1017.
[57] Jiang X, Stockwell BR, Conrad M. Ferroptosis: mechanisms, biology and role in disease. Nature Reviews. Molecular Cell Biology. 2021; 22: 266–282.
[58] Zhu H, Tan J, Wang Z, Wu Z, Zhou W, Zhang Z, *et al*. Bioinformatics analysis constructs potential ferroptosis-related ceRNA network involved in the formation of intracranial aneurysm. Frontiers in Cellular Neuroscience. 2022; 16: 1016682.
[59] Starke RM, Chalouhi N, Ali MS, Jabbour PM, Tjoumakaris SI, Gonzalez LF, *et al*. The role of oxidative stress in cerebral aneurysm formation and rupture. Current Neurovascular Research. 2013; 10: 247–255.
[60] Starke RM, Thompson JW, Ali MS, Pascale CL, Martinez Lege A, Ding D, *et al*. Cigarette Smoke Initiates Oxidative Stress-Induced Cellular Phenotypic Modulation Leading to Cerebral Aneurysm Pathogenesis. Arteriosclerosis, Thrombosis, and Vascular Biology. 2018; 38: 610–621.
[61] Pascale CL, Martinez AN, Carr C, Sawyer DM, Ribeiro-Alves M, Chen M, *et al*. Treatment with dimethyl fumarate reduces the formation and rupture of intracranial aneurysms: Role of Nrf2

activation. Journal of Cerebral Blood Flow and Metabolism. 2020; 40: 1077–1089.
[62] Cheng XM, Hu YY, Yang T, Wu N, Wang XN. Reactive Oxygen Species and Oxidative Stress in Vascular-Related Diseases. Oxidative Medicine and Cellular Longevity. 2022; 2022: 7906091.
[63] Zheng D, Liu J, Piao H, Zhu Z, Wei R, Liu K. ROS-triggered endothelial cell death mechanisms: Focus on pyroptosis, parthanatos, and ferroptosis. Frontiers in Immunology. 2022; 13: 1039241.
[64] Sampilvanjil A, Karasawa T, Yamada N, Komada T, Higashi T, Baatarjav C, *et al*. Cigarette smoke extract induces ferroptosis in vascular smooth muscle cells. American Journal of Physiology. Heart and Circulatory Physiology. 2020; 318: H508–H518.
[65] Zhang S, Bei Y, Huang Y, Huang Y, Hou L, Zheng XL, *et al*. Induction of ferroptosis promotes vascular smooth muscle cell phenotypic switching and aggravates neointimal hyperplasia in mice. Molecular Medicine. 2022; 28: 121.
[66] Ji QX, Zeng FY, Zhou J, Wu WB, Wang XJ, Zhang Z, *et al*. Ferroptotic stress facilitates smooth muscle cell dedifferentiation in arterial remodelling by disrupting mitochondrial homeostasis. Cell Death and Differentiation. 2023; 30: 457–474.
[67] Jin R, Yang R, Cui C, Zhang H, Cai J, Geng B, *et al*. Ferroptosis due to Cystathionine γ Lyase/Hydrogen Sulfide Downregulation Under High Hydrostatic Pressure Exacerbates VSMC Dysfunction. Frontiers in Cell and Developmental Biology. 2022; 10: 829316.
[68] Yang Y, Klionsky DJ. Autophagy and disease: unanswered questions. Cell Death and Differentiation. 2020; 27: 858–871.
[69] Sun L, Zhao M, Zhang J, Lv M, Li Y, Yang X, *et al*. MiR-29b Downregulation Induces Phenotypic Modulation of Vascular Smooth Muscle Cells: Implication for Intracranial Aneurysm Formation and Progression to Rupture. Cellular Physiology and Biochemistry. 2017; 41: 510–518.
[70] Sun L, Zhao M, Liu A, Lv M, Zhang J, Li Y, *et al*. Shear Stress Induces Phenotypic Modulation of Vascular Smooth Muscle Cells via AMPK/mTOR/ULK1-Mediated Autophagy. Cellular and Molecular Neurobiology. 2018; 38: 541–548.
[71] Li T, Tan X, Zhu S, Zhong W, Huang B, Sun J, *et al*. SPARC induces phenotypic modulation of human brain vascular smooth muscle cells via AMPK/mTOR-mediated autophagy. Neuroscience Letters. 2019; 712: 134485.
[72] Kim YC, Guan KL. mTOR: a pharmacologic target for autophagy regulation. The Journal of Clinical Investigation. 2015; 125: 25–32.
[73] Liu M, Zhao J, Zhou Q, Peng Y, Zhou Y, Jiang Y. Primary Cilia Deficiency Induces Intracranial Aneurysm. Shock. 2018; 49: 604–611.
[74] Rouer M, Xu BH, Xuan HJ, Tanaka H, Fujimura N, Glover KJ, *et al*. Rapamycin limits the growth of established experimental abdominal aortic aneurysms. European Journal of Vascular and Endovascular Surgery. 2014; 47: 493–500.
[75] Chen Y, He Y, Wei X, Jiang DS. Targeting regulated cell death in aortic aneurysm and dissection therapy. Pharmacological Research. 2022; 176: 106048.
[76] Hou J, Hsu JM, Hung MC. Molecular mechanisms and functions of pyroptosis in inflammation and antitumor immunity. Molecular Cell. 2021; 81: 4579–4590.
[77] Yuan J, Amin P, Ofengeim D. Necroptosis and RIPK1-mediated neuroinflammation in CNS diseases. Nature Reviews. Neuroscience. 2019; 20: 19–33.
[78] Deretic V. Autophagy in inflammation, infection, and immunometabolism. Immunity. 2021; 54: 437–453.
[79] Chen X, Kang R, Kroemer G, Tang D. Ferroptosis in infection, inflammation, and immunity. The Journal of Experimental Medicine. 2021; 218: e20210518.
[80] Muhammad S, Chaudhry SR, Dobreva G, Lawton MT, Niemelä M, Hänggi D. Vascular Macrophages as Therapeutic Targets to Treat Intracranial Aneurysms. Frontiers in Immunology. 2021; 12: 630381.
[81] Chalouhi N, Theofanis T, Starke RM, Zanaty M, Jabbour P, Dooley SA, *et al*. Potential role of granulocyte-monocyte colony-stimulating factor in the progression of intracranial aneurysms. DNA and Cell Biology. 2015; 34: 78–81.